

Metabolic Regulatory Network Kinetic Modeling with Multiple Isotopic Tracers for iPSCs

Keqi Wang^a, Wei Xie^{a,*} and Sarah W. Harcum^{b,*}

^aDepartment of Mechanical and Industrial Engineering, Northeastern University, Boston, MA, USA

^bDepartment of Bioengineering, Clemson University, Clemson, SC, USA

ARTICLE INFO

Keywords:

Cell Therapy Manufacturing
Induced Pluripotent Stem Cells
Process Dynamic Model
Stable Isotope Labeling

ABSTRACT

The rapidly expanding market for regenerative medicines and cell therapies highlights the need to advance the understanding of cellular metabolisms and improve the prediction of cultivation production process for human induced pluripotent stem cells (iPSCs). In this paper, a metabolic kinetic model was developed to characterize underlying mechanisms of iPSC culture process, which can predict cell response to environmental perturbation and support process control. This model focuses on the central carbon metabolic network, including glycolysis, pentose phosphate pathway (PPP), tricarboxylic acid (TCA) cycle, and amino acid metabolism, which plays a crucial role to support iPSC proliferation. Heterogeneous measures of extracellular metabolites and multiple isotopic tracers collected under multiple conditions were used to learn metabolic regulatory mechanisms. Systematic cross-validation confirmed the model's performance in terms of providing reliable predictions on cellular metabolism and culture process dynamics under various culture conditions. Thus, the developed mechanistic kinetic model can support process control strategies to strategically select optimal cell culture conditions at different times, ensure cell product functionality, and facilitate large-scale manufacturing of regenerative medicines and cell therapies.

1. Introduction

Cell therapeutics and regenerative medicines have the potential to treat and prevent diseases, such as cancers, and cardiovascular and hematologic diseases (Hanna et al., 2016; Stephanopoulos et al., 1998). The cell therapy market is experiencing unparalleled growth and the projected worth of the relevant market is expected to be over \$8 billion in 2025 (Fiorenza et al., 2020). To meet the rising demand, cost reductions in manufacturing and increases in quality for human induced pluripotent stem cells (iPSCs) on a large scale are crucial for the success of cell therapies (Odenwelder et al., 2021). Unlike traditional biopharmaceuticals, the cells are the product with functional identity depending on the regulatory metabolic dynamic behaviors.

The efficacy of the cells is very sensitive to culture conditions. Variability in the culture conditions can lead to reduced yields and heterogeneous cell populations. Heterogeneous cell populations have been observed to increase the potential for tumor or teratoma formulation in the patient (Dressel, 2011). Traditional cell culture process control strategies often are ad hoc and rely solely on experimental approaches or PID controllers ignoring long-term effects. The optimal design and control of mammalian cell culture processes, especially iPSCs, can be laborious due to the limited understanding of cellular metabolisms and end-to-end cultivation process dynamics (Kyriakopoulos et al., 2018; Wang et al., 2021).

In order to determine the best culture conditions, accounting for cell life cycle, relationships between culture conditions and the output trajectory (i.e., cell functional identity and yield) are needed. Mechanistic dynamics models have the capability to predict cell outcomes (e.g., metabolic flux rates), which can be used to assess product quality. These models provide systems-level descriptions of metabolic networks and regulatory mechanisms. With this complex and high-level cellular description, it is possible to interface such models with process control algorithms to strategically select the optimal culture conditions at different times.

The proposed model for the iPSC metabolic network and regulation mechanisms combines four modeling approaches to leverage the strengths of each approach: (1) metabolic flux analysis (MFA), (2) flux balance analysis (FBA), (3) ¹³C-MFA, and (4) kinetic models. In MFA, metabolic flux rates (such as substrate uptake rate and metabolite secretion rate) are estimated based on experimental measurements subject to stoichiometric constraints. Under the standard assumption of (pseudo) steady state for intracellular metabolites, the sum of all fluxes producing a metabolite is equal to the sum of all fluxes consuming that metabolite. This technique is frequently used to compare the metabolism of different cell lines to assess the activity of individual pathways under different cultivation conditions (Niklas and Heinze, 2012). However, intracellular metabolites can change during cell proliferation (Templeton et al., 2013).

Stable isotope studies, integrating with MFA, have provided more detailed information on intracellular state and metabolic pathways, namely ¹³C-MFA can precisely estimate metabolic reaction rates. Typically these flux rates are estimated from measured isotopic distributions (MID)

*Corresponding author

E-mail: w.xie@northeastern.edu (W. Xie); harcum@clemson.edu (S.W. Harcum)

ORCID(s): 0000-0001-9563-4927 (W. Xie)

patterns and external metabolites concentrations, which requires the assumption of isotopic and metabolic steady state (Antoniewicz, 2015, 2018; Rivera-Ordaz et al., 2021; Sen-gupta et al., 2011). Several modeling tools (Leighty and Antoniewicz, 2011; Antoniewicz, 2015, 2018) can predict fluxes for cultures that have not reached isotopic and/or fluxes steady state. However, these tools are not easily integrated into the process control of iPSC cultures.

Another approach to model cell dynamics includes kinetic-metabolic models (Kyriakopoulos et al., 2018). The vast majority of the kinetic models use Monod and Michaelis–Menten expression formalisms modeling the metabolic regulation mechanisms (Ghorbaniaghdam et al., 2014a, 2013, 2014b; Kyriakopoulos et al., 2018; Nolan and Lee, 2011). For Chinese hamster ovary (CHO) cell cultures, kinetic-metabolic models include glycolysis, pentose phosphate pathway (PPP), tricarboxylic acid (TCA) cycle, respiratory chain, as well as the regulatory functions from energy shuttles (ATP/ADP) and cofactors (NADH, NAD⁺, NADPH, NADP⁺); this high level of details is required to predict hypoxic perturbation (Ghorbaniaghdam et al., 2013, 2014b). For example, Nolan and Lee (2011) proposed a Monod model that characterizes the cell flux rate response to environmental perturbation. That study used limiting substrate kinetics to calculate the extracellular metabolite consumption/production rates and further infer metabolic flux rates built on a static MFA assumption, i.e., assuming the intracellular metabolites are at the pseudo-steady state. Even though several *in silico* metabolomic platforms have been developed for CHO cells (Ghorbaniaghdam et al., 2014a, 2013, 2014b; Kyriakopoulos et al., 2018; Nolan and Lee, 2011), a metabolic regulatory network simulator for iPSC has not been developed.

To gain a better understanding of cell behavior in aggregates, the objective of this study was to develop and validate an iPSC metabolic regulatory network mechanistic model capability of predicting cell responses to environmental perturbations. Due to strong cell-cell interactions and extracellular matrix secretion, self-aggregation compact cell spheres naturally form. In large aggregates nutrients limitations and high metabolic waste concentrations can occur. This issue can be more serious for large-scale bioreactors.

To support the prediction of iPSC response to environmental perturbations occurring during the culture process, the proposed model focused on the central metabolism since it plays a critical role in stem cell proliferation, biosynthesis, and functionality. The developed mechanistic model incorporated time-variate dynamics and regulatory mechanisms. This model used previously obtained experimentally MIDs for iPSC cultures to estimate model parameters for the time-variate reactions and regulatory mechanisms. During the model development, the level of detail required for key pathways was explored, namely the PPP and branched amino acids uptake rates into the TCA cycle. The model development and final model details will be presented with comparisons to the experimental data. Note the proposed model

structure could be readily adapted to other mammalian cell culture systems.

2. Data Description

Briefly, the data used to obtain model parameters were from an experimental study of K3 iPSCs that included extracellular metabolite and isotopic labeling information for four culture conditions using three tracers: glucose, glutamine and lactate. (Odenwelder et al., 2021). The four different initial culture media concentrations were: (1) high glucose and low lactate (HGLL); standard initial conditions, i.e., 18.3 mM glucose and 0 mM lactate; (2) high glucose and high lactate (HGHL), i.e., 18.3 mM glucose and 20 mM lactate; (3) low glucose and low lactate (LGLL), i.e., 5.6 mM glucose and 0 mM lactate; and (4) low glucose and high lactate (LGHL), i.e., 5.6 mM glucose and 20 mM lactate. These condition concentrations were selected such that the growth rate was similar for all conditions.

Cell density, glucose, lactate, pyruvate, and extracellular amino acid concentrations were obtained for each condition at 0-, 12-, 24-, 36-, and 48-h. Intracellular amino acid MIDs are obtained from parallel labeling experiments that used [1,2-¹³C₂] glucose, [U-¹³C₅] L-glutamine, and [U-¹³C₃] sodium L-lactate (when lactate was added to culture media). A schematic of the time-course measurements as shown in Figure 1 were used to develop the metabolic regulatory network kinetic model for iPSC culture process.

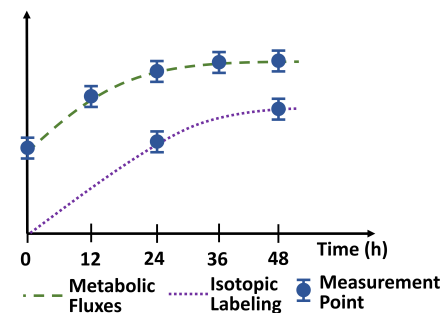


Figure 1: A schematic of the time-course extracellular concentrations measurements and isotopic intracellular amino acid MIDs for the experimental iPSC cultures. Metabolics were measured every 12 h, while the MIDs were only obtained at 24- and 48-h. The 24-h MIDs were considered to be at metabolic steady-state, but not isotopic steady-state, while by 48-h, both metabolic and isotopic steady-state were reached.

3. Model Development

The iPSC metabolic regulatory network kinetic model will be presented by the four levels of development. Section 3.1 provides the general dynamic model description, including (1) regulatory metabolic network kinetic modeling; and (2) time-course isotopic labeling simulation. Section 3.2 presents the iPSC metabolic reaction network which includes central carbon metabolism. In Section 3.3, metabolic flux kinetics, characterizing cell response to environmental

perturbations, were learned from time-course extracellular concentration measurements and MIDs. Finally, in Section 3.4, the assessment of fit and validation of the dynamic model for the iPSC cultures is discussed, where the objective function and goodness-of-fit will be presented.

3.1. Metabolic Network Kinetic Modeling

In this section, the general regulatory metabolic network kinetic model and time-course isotopic labeling simulation are presented. The kinetic model captures the dynamic changes in cell density, and extracellular and intracellular metabolite concentrations, where the changing rates of metabolites depend on the concentration of substrates and inhibitors. To incorporate the mass isotopic data, a dynamic isotopic labeling system was constructed, and a time-course isotopic labeling simulation was developed. Overall, the metabolic reaction network kinetic model provides a comprehensive understanding of the underlying mechanisms of the iPSC culture process.

(1) Metabolic Reaction Network Kinetic Model. The data from the study for K3 iPSCs were collected during the exponential growth phase (Odenwelder et al., 2021). By experimental design, the specific cell growth rates, denoted by $\mu(\text{h}^{-1})$, were determined to be constant for the four batch culture conditions, i.e., HGLL, HGHL, LGLL, and LGHL. Thus the classical cell density formalism was used to relate growth and the cell density, denoted by $X(t)$ (cells/cm²), at time t as,

$$\frac{dX(t)}{dt} = \mu X(t). \quad (1)$$

The extracellular metabolite concentrations at time t are denoted by a vector with dimension p , i.e., $\mathbf{s}(t) = (s_1(t), s_2(t), \dots, s_p(t))^\top$. Similarly, the intracellular metabolite concentrations of interest are denoted by a vector with dimension q at time t as $\mathbf{\ell}(t) = (\ell_1(t), \ell_2(t), \dots, \ell_q(t))^\top$. Thus, at any time t , the state of extracellular and intracellular metabolite concentrations is denoted by

$$\mathbf{u}(t) = (\mathbf{s}(t)^\top, \mathbf{\ell}(t)^\top)^\top.$$

To model the dynamic evolution of cell response to environmental perturbation during the iPSC culture process, at any time t , the specific reaction flux rates represented by a vector of with dimension n depend on the extracellular and intracellular metabolite concentrations, i.e.,

$$\mathbf{v}[\mathbf{u}(t)] = (v_1[\mathbf{u}(t)], v_2[\mathbf{u}(t)], \dots, v_n[\mathbf{u}(t)])^\top.$$

Let N denote a $(p+q) \times n$ stoichiometry matrix characterizing the structure of metabolic reaction network. Therefore, the dynamic evolution of extracellular and intracellular metabolite concentrations is modelled through a mass balance on the system of equations,

$$\frac{d\mathbf{u}(t)}{dt} = N\mathbf{v}[\mathbf{u}(t)]X(t). \quad (2)$$

(2) Regulatory Mechanism Modeling and Learning.

To capture the cell response to environmental perturbation, a Michaelis–Menten (MM) formalism based regulation model was used to characterize the relationship of metabolic flux rates depending on the concentrations of associated substrates and inhibitors. This allows leveraging the existing biology knowledge and facilitating the learning of regulation mechanisms of iPSC metabolic reaction network from the experimental data.

Specifically, the g -th flux rate at the time t is modeled as,

$$v_g[\mathbf{u}(t)] = v_{max,g} \prod_{y \in \Omega_Y^g} \frac{u_y(t)}{u_y(t) + K_{m,y}} \prod_{z \in \Omega_Z^g} \frac{K_{i,z}}{u_z(t) + K_{i,z}}, \quad (3)$$

for $g = 1, 2, \dots, n$, where the set Ω_Y^g represents the collection of activators (such as nutrients and substrates) influencing the flux rate v_g and the set Ω_Z^g represents the collection of inhibitors dampening v_g . The parameters $K_{i,z}$, $K_{m,y}$, and $v_{max,g}$ represent the affinity constant, the inhibition constant, and the maximum specific flux rate respectively. For iPSC cultures, the experimental data referenced were used to identify the critical activators and inhibitors, as well as learning the MM model coefficients.

(3) Time-Course Isotopic Labeling Simulation. Different ¹³C-labeling patterns are generated by different flux distributions $\mathbf{v}[\mathbf{u}(t)]$. Thus, incorporating the dynamic system of isotopic labeling patterns (MID), which is a vector containing the fractional abundance of each mass state of metabolites, into the metabolic network kinetic model can aid in understanding intercellular metabolic network mechanisms. However, modeling each individual atom as one system state variable is computationally expensive. To address this issue, the elementary metabolite unit (EMU) framework was proposed, and it is based on a highly efficient decomposition method that can identify the minimum amount of information needed to simulate isotopic labeling (Antoniewicz et al., 2007). Basically, the EMUs are created by using a decomposition algorithm and form the new basis for generating system equations that describe the relationship between fluxes and isotope measurements; see more detailed information in studies, such as Ahn and Antoniewicz (2011, 2013); Antoniewicz (2015, 2021); Antoniewicz et al. (2007); Antoniewicz (2018); Jazmin and Young (2013).

Based on the study (Antoniewicz et al., 2007; Young et al., 2008), the reduced system can be obtained after decoupling based on EMUs with size $r = 1, 2, \dots, R$ and connectivity. The time-dependent network was first identified: the decoupled EMUs with size r network, $G_r(t) = \{V_r, E_r, W_r(t)\}$ with $r = 1, 2, \dots, R$. The vector $V_r = (V_r^{(a)^\top}, V_r^{(b)^\top})^\top$ is the set of vertices (i.e., EMUs) within the r -th network, the vector $V_r^{(b)}$ with dimension $|V_r^{(b)}|$ is the set of input EMUs (i.e., EMUs with size smaller than r or EMUs of extracellular carbon sources), the vector $V_r^{(a)}$ with dimension $|V_r^{(a)}|$ is the set of EMUs with size r . E_r is the adjacency matrix with dimension $(|V_r^{(a)}| + |V_r^{(b)}|) \times (|V_r^{(a)}| +$

$|V_r^{(b)}|$) representing the dependence between each vertex. The corresponding weight matrix $W_r(t)$ varies with time t . The non-negative (i, j) -th element $W_r^{(i,j)}(t)$ indicates the flux rate of the reaction producing i -th EMU by consuming j -th EMU at time t .

Thus, at any time t , the dynamic isotopic labeling system can be defined as:

$$C'_r(t) = \frac{A_r(t) \cdot C_r(t) + B_r(t) \cdot D_r(t)}{P_r(t)} \quad (4)$$

where the rows of the state matrix $C_r(t)$ correspond to the MIDs of EMUs within $V_r^{(a)}$ at time t . The input matrix $D_r(t)$ is analogous but with rows of input/carbon sources EMUs within $V_r^{(b)}$ at time t . The concentration matrix $P_r(t)$ is a diagonal matrix whose elements are pool sizes corresponding to EMUs represented in $V_r^{(a)}$. The construction of $A_r(t)$ and $B_r(t)$ are based on the decoupled EMU reaction network $G_r(t)$. The system matrix $A_r(t)$ with size $|V_r^{(a)}| \times |V_r^{(a)}|$ and matrix $B_r(t)$ with size $|V_r^{(a)}| \times |V_r^{(b)}|$ describe the metabolic network with elements defined as follows:

$$A_r^{(i,j)}(t) = \begin{cases} - \sum_{k=1}^{|V_r^{(a)}|} W_r^{(k,j)}(t), & i = j, \\ W_r^{(i,j)}(t), & i \neq j; \end{cases} \quad (5)$$

and

$$B_r^{(i,j)}(t) = W_r^{(i,|V_r^{(a)}|+j)}(t). \quad (6)$$

3.2. iPSC Metabolic Reaction Network

The developed iPSC metabolic network model leverages central carbon metabolism from several previously published metabolic frameworks (Dressel, 2011; Fiorenza et al., 2020; Ghorbaniaghdam et al., 2014b; Niklas and Heinze, 2012; Ghorbaniaghdam et al., 2013; Odenwelder et al., 2021) and further learns from data. The iPSC metabolic network included glycolysis, TCA cycle, anaplerosis, PPP, and amino acid metabolism. For simplification, the reactions of PPP were collapsed into two reactions: Oxidative phase/branch and Non-oxidative phase/branch (i.e., No. 9 & 10 reaction in Table 2). During the exponential phase, greater than 90% of pentose-phosphate carbons is returned to glycolysis for the mammalian cell (Templeton et al., 2013; Halestrap, 2012). Thus, the synthesis of nucleotides and nucleic acids is considered an insignificant contributor to the model. The metabolic network is shown in Fig. 2 and the metabolic stoichiometry is listed in Table 2. The descriptions of metabolites and the enzymes conform to the Enzyme Commission Number (EC-No.) and are provided in Tables 4 and 5, respectively.

3.3. Biokinetic Model of Flux Regulatory Mechanism

Due to the lack of energetic state and redox level measurements, each metabolic flux rate is modeled as dependent on the substrates and inhibitors concentrations using

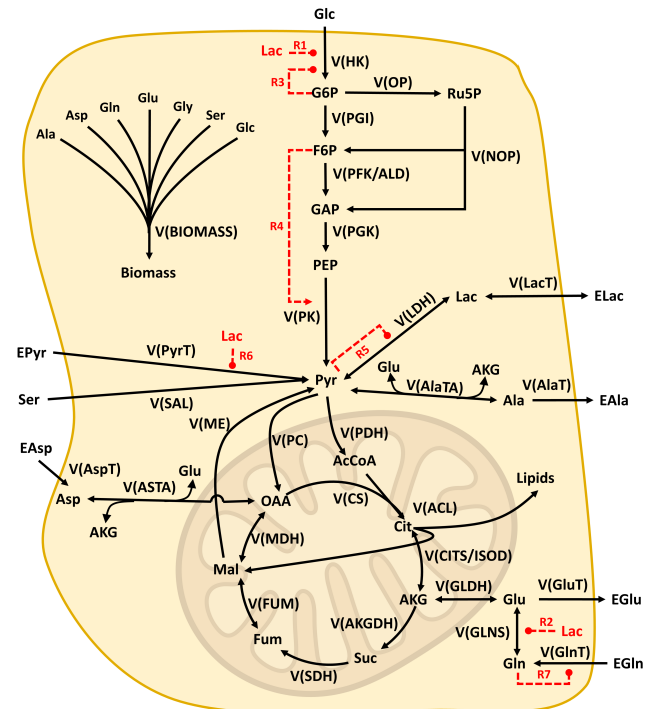


Figure 2: The iPSC regulatory metabolic network. Glycolysis, PPP, TCA and anaplerosis and amino acid utilization are shown. Additionally, the regulatory mechanisms included in the dynamic model are shown. The metabolites descriptions are listed in Table 4. The enzyme description, including the Enzyme Commission Numbers (EC-No.) for each reaction, is listed in Table 5.

Michaelis–Menten model formalism. Similar to the existing studies (Dressel, 2011; Fiorenza et al., 2020; Ghorbaniaghdam et al., 2014b), for simplification purposes and also due to a lack of available data in the literature, a single affinity constant value is used for each metabolite. Additionally, reaction reversibility was considered during the iPSC culture model development for some key reactions. The final model is fully described in Table 3. Several regulatory mechanisms (i.e., No. **R1** to **R7**) are highlighted in Fig. 2, which were incorporated into the metabolic flux kinetics model to improve the model's prediction capability and better characterize the responses to environmental perturbations. These key final reactions are described below, where these new dependencies are highlighted in under brackets with the corresponding regulatory mechanism No., while the original nomenclature is outside the brackets.

- Lactate accumulation has previously been reported to reduce glycolytic activity by inhibiting hexokinase (HK) and phosphofructokinase (PFK) activity in mammalian cells, where lactate acts as a signaling molecule to down-regulate PFK activity (Ivarsson et al., 2015; Mulukutla et al., 2012; Costa Leite et al., 2007). After evaluation of the experimental data, the model for HK was updated to include this inhibitory

effect of lactate on it:

$$v(HK) = v_{max,HK} \times \frac{Glc}{K_{m,Glc} + Glc} \times \underbrace{\frac{K_{i,LactoHK}}{K_{i,LactoHK} + Lac}}_{R1}. \quad (7)$$

- Since lactate inhibits glutaminase activity – the enzyme responsible for converting glutamine (GLN) to glutamate (GLU) (Glacken et al., 1988; Hassell et al., 1991) – the forward (*f*) flux rate for the reaction, i.e., $Gln \leftrightarrow Glu + NH_4$, was updated,

$$v(GLNSf) = v_{max,fGLNS} \times \frac{Gln}{K_{m,Gln} + Gln} \times \underbrace{\frac{K_{i,LactoGLNS}}{K_{i,LactoGLNS} + Lac}}_{R2}. \quad (8)$$

- Several regulatory functions, adapted from Ghorbani-aghdam et al. (2013, 2014a,b), were evaluated using the experimental data to characterize activations and inhibitions. The regulatory mechanisms involved in glycolysis are described as: a) hexokinase inhibition by its product G6P, see R3 in eq (9); b) activation of pyruvate kinase by F6P, see R4 in eq (10), as well as c) the inhibition of lactate dehydrogenase reverse (*r*) reaction, see R5 in eq (11), was changed to include the G6P inhibition:

$$v(HK) = v_{max,HK} \times \frac{Glc}{K_{m,Glc} + Glc} \times \underbrace{\frac{K_{i,LactoHK}}{K_{i,LactoHK} + Lac}}_{R3} \times \underbrace{\frac{K_{i,G6P}}{K_{i,G6P} + G6P}}_{R3}; \quad (9)$$

$$v(PK) = v_{max,PK} \times \frac{PEP}{K_{m,PEP} \times \left[1 + \frac{K_{a,F6P}}{F6P} \right] + PEP}; \quad (10)$$

$$v(LDHr) = v_{max,rLDH} \times \frac{Lac}{K_{m,Lac} + Lac} \times \underbrace{\frac{K_{i,Pyr}}{K_{i,Pyr} + Pyr}}_{R5}. \quad (11)$$

- Both lactate and pyruvate transport across the plasma membrane are facilitated by proton-linked monocarboxylate transporters (MCTs) (Halestrap, 2012; Huckabee, 1956). More favorable lactate transport kinetics may decrease pyruvate consumption under high lactate culture conditions (Odenwelder et al., 2021; Draoui and Feron, 2011). Thus, the model of PyrT was updated to:

$$v(PyrT) = v_{max,PyrT} \times \frac{EPyr}{K_{m,EPyr} + EPyr} \times \underbrace{\frac{K_{i,LactoPyr}}{K_{i,LactoPyr} + Lac}}_{R6}. \quad (12)$$

- Since the transportation of extracellular-glutamine via cell membrane can be inhibited by intracellular-glutamine, the model for GlnT was updated to:

$$v(GlnT) = v_{max,GlnT} \times \frac{EGln}{K_{m,EGln} + EGln} \times \underbrace{\frac{K_{i,GLN}}{K_{i,GLN} + GLN}}_{R7}. \quad (13)$$

3.4. Model Fit and Goodness-of-fit Assessment

The proposed iPSC metabolic network kinetic model focused on the characterization of central carbon metabolism and regulation mechanisms under different cultural environments, i.e., different levels of glucose and lactate concentrations. It is well known that in iPSC aggregate cultures, the glucose concentration will be low at the aggregate center and the lactate concentration will be high (Kinney et al., 2011), as its proper functioning is critical for the survival and proliferation of iPSCs (Nelson et al., 2008), as well as cell product quality assurance. The final model developed is shown in Table 2. This model includes 30 metabolic reactions with 32 variables (metabolites' concentration) in the reaction equations. The kinetic formulations for the flux regulation are presented in Table 3.

The proposed iPSC culture kinetic model estimates model parameters using the extracellular and MID data collected over time under the four different culture conditions. Denote the available extracellular metabolites concentrations data at time t as s_t^{meas} for $t = 0, 12, 24, 36, 48$ hour. Denote intracellular isotopic labeling measurements at time t' as $MID_{t'}^{meas}$ for $t' = 24, 48$ hour. For the model fitting, the objective is minimizing the weighted sum of squared residuals (SSR) between available experimental data (s_t^{meas} , $MID_{t'}^{meas}$) and model predicted values (s_t^{sim} , $MID_{t'}^{sim}$),

$$\min SSR = \sum_{t=1}^T \frac{(s_t^{sim} - s_t^{meas})^2}{var_t^s} + \sum_{t'=1}^{T'} \frac{(MID_{t'}^{sim} - MID_{t'}^{meas})^2}{var_{t'}^M}, \quad (14)$$

where the weight is the inverse of the variance of the experimental measurements so that the model can systematically fit the metabolic regulation network well at different times.

The initial conditions for extracellular metabolites were obtained from culture data. As the experimental data only include the relative abundance and the MIDs, estimates for the initial intracellular metabolite concentrations were sourced from the literature for mammalian cells cultured under similar conditions (Chang et al. (2021) and references therein). The initial kinetic parameter values were taken from literature for similar metabolic networks and pathways (Chang et al. (2021) and references therein).

The goodness-of-fit for the developed iPSC metabolic kinetic model was assessed based on predictions using a chi-square test. Basically, the null hypothesis is that the fitted model can faithfully represent the iPSC culture metabolic mechanism. This test assumes that the minimized variance-weighted SSR follows a chi-square distribution with d degrees of freedom, where the degree of freedom d equals the number of observations minus the number of fitted parameters. In this study, $p > 0.05$ indicates the model predictions are not significantly different than the measured values for the chi-square statistical test.

4. Results and Discussion

The simulator was estimated with limited experimental data and then validated in two manners. First, to mimic the dynamic data collection and assess the rolling forecasts required for process control, at any time t , the historical data were used to predict into the future. In Section 4.1, the model's ability to capture the dynamic evolution of iPSC metabolic characteristics was evaluated. The model was trained on experimental data collected over different time intervals (0-h to 12-h, 0-h to 24-h, and 0-h to 36-h), and used to predict the iPSC culture for up to 48-h. Second, to assess the model's ability to generalize and extrapolate to new conditions, three datasets, randomly selected from (1) high glucose and low lactate (HGLL); (2) high glucose and high lactate (HGHL); (3) low glucose and low lactate (LGLL); and (4) low glucose and high lactate (HGHL), were used to predict the fourth dataset with different initial conditions in Section 4.2. Basically, three of the conditions were used to train the model, then the fourth with different initial conditions was predicted. The four culture conditions were each examined in succession. Therefore, by validating the model's prediction performance under different experimental conditions, its robustness and usefulness for predicting iPSC characteristics in a variety of settings is verified.

4.1. Prediction of iPSC Culture Process

During the model validation process, the proposed model simulator was trained using experimental data collected over various time intervals (0-h to 12-h, 0-h to 24-h, and 0-h to 36-h). The model's ability to predict the dynamic trajectories of key metabolites, including glucose, lactate, glutamate, glutamine, and pyruvate, as well as cell density, was evaluated by comparing the predicted values to

experimental observations up to 48 hours. Fig. 3 provides a representative result of the cell culture process prediction for the case starting with HGLL. The results for the remaining settings, including HGHL, LGLL, and LGHL, are presented in Appendix Fig. 8 to 10. The chi-square tests conducted on different time intervals were used to assess the goodness-of-fit of the predictive models. The prediction test statistics for the model trained on 0-12 hours of experimental data was 33.6 with 47 degrees of freedom (p -value = 0.93), while the test statistics for the model trained on 0-24 hours and 0-36 hours of experimental data were 82.6 with 107 degrees of freedom (p -value = 0.96) and 138.1 with 167 degrees of freedom (p -value = 0.95), respectively. All of the p -values are much greater than 0.05, which indicates the proposed metabolic kinetics simulator fits well with the experimental dataset. The results in Fig. 3 demonstrate that the fitted model can provide better predictions for most of the metabolite trajectories as more data are collected in time.

Overall, the predicted profiles of the iPSC cultures can closely track the dynamic patterns of the measured profiles and capture the cell culture dynamics. The experimental iPSC data were obtained from plates and dishes with limited space. Even though the overall growth rates were the same across the four conditions by experimental design, the growth rate decreased with time as nutrients were consumed and metabolic wastes accumulated. It is important to note that the developed mechanistic metabolic kinetic model is a simplified representation of the iPSC carbon central network, there could likely be some key metabolic regulations and biochemical reactions that were not incorporated; but they might be included for aggregate cultures. The less accurate predictive performances for lactate (under low lactate conditions) and glutamate may be due to the omission of key reactions or regulatory functions. For example, as suggested by the calibrated model in previous studies (Ghorbaniaghdam et al., 2013, 2014a,b), the membrane transportation of glutamate for mammalian cells is significantly impacted by the energetic state (ATP and ADP), and the forward and reverse conversion of lactate to pyruvate is influenced by the redox level (NAD and NADH).

Since the redox level and energetic state-related measurements were not collected for these iPSC cultures, these factors were not accounted for in the current model. Nolan and Lee (2011) found for CHO cells, a redox parameter assisted with lactate predictions; however, the redox parameter implemented by Nolan and Lee (2011) was unmeasurable and thus would be difficult to incorporate into a control model. Furthermore, the lower prediction performance for glutamate may be attributed to its involvement in multiple reactions (see Fig. 2), leading to error accumulation over time. Future work should address these limitations with more comprehensive experimental data for iPSC cultures.

4.2. Prediction across Different Initial Conditions

In order to understand how iPSC responds to different cultural conditions (i.e., variable glucose and lactate), cross validation was used, where one dataset is left out

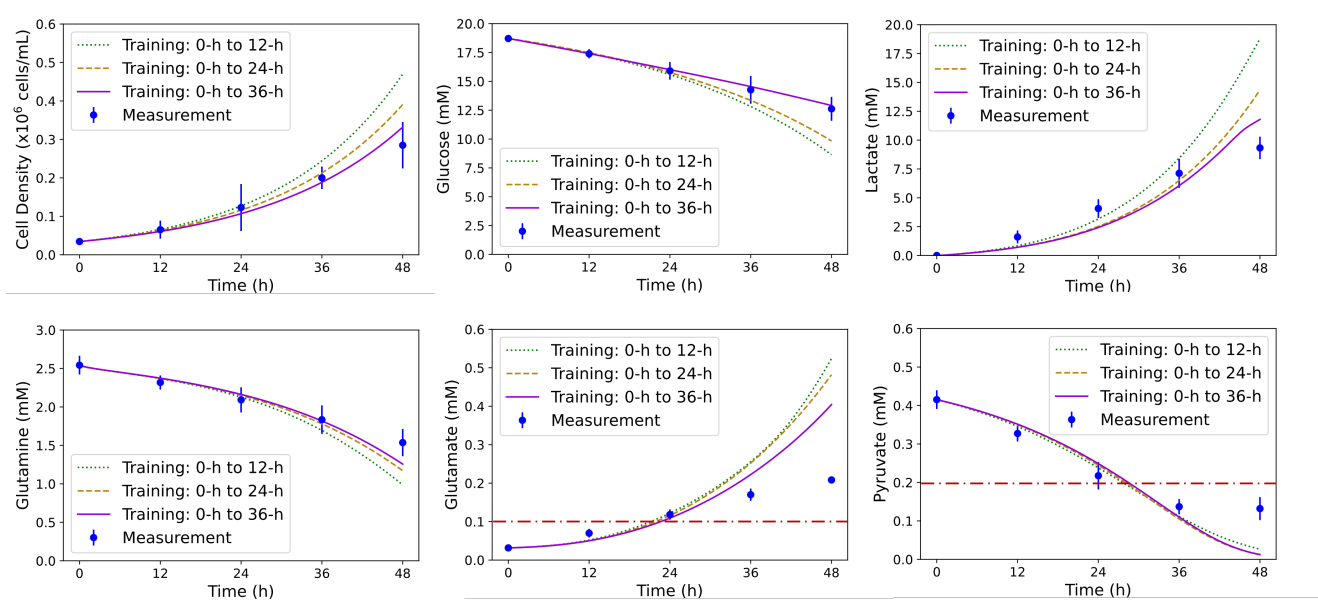


Figure 3: Cell characteristic predictions for the high glucose and low lactate cultures using the dynamic model trained on different time intervals. (A) Cell density, (B) Glucose, (C) Lactate, (D) Glutamine, (E) Glutamate, and (F) Pyruvate. Times 0-h to 12-h (green dotted line); Times 0-h to 24-h (brown dashed line); and Times 0-h to 36-h (purple solid line). The detection limit of the Cedex Bioanalyzer is shown as the red dash-dot line.

while training the model with data from the remaining three datasets. Fig. 4 shows the results of this cross training approach for the HGHL cultures where the HGHL, LGHL, and LGHL datasets were used. Cell density and key metabolites (i.e., glucose, lactate, glutamate, glutamine, and pyruvate) were predicted and are shown with the average of the measured values with standard deviations. The across-condition extrapolation predictions for other culture conditions are provided in Appendix Fig. 11 to 13. To evaluate the goodness-of-fit, the chi-square test SSR statistics is 783 with 802 degrees of freedom with p -value = 0.67 much greater than 0.05. This p -value indicates that the metabolic kinetic model can faithfully represent the iPSC culture regulatory mechanisms under different levels of glucose and lactate concentrations.

The predictions of intracellular MID from the [1,2-¹³C₂] glucose and [U-¹³C₅] glutamine tracer at 48-h under the control (HGHL) culture condition are shown in Fig. 5 and Fig. 6, respectively. Even though there is some prediction error, the simulation model can correctly predict the dynamics and interdependencies of multivariate iPSC culture process metabolism. The developed metabolic kinetic model can faithfully predict the cell response to environmental perturbation, which could guide the strategic feeding strategy for the integrated iPSC culture process for future research. In addition, by incorporating even the simplified PPP reactions, the M+1 isotopic labeling pattern for pyruvate and related metabolites from [1,2-¹³C₂] glucose tracer can be well-predicted.

The prediction of metabolic flux maps for K3 iPSC under control culture at 24-h and 48-h are shown in Fig. 7. The

prediction performance of metabolic concentration trajectory and flux maps for K3 iPSC under HGHL, LGHL, and LGHL are provided in Appendix Fig. 14 to Fig. 16. Since no restrictive steady-state assumption was required for the developed metabolic kinetic model, the flow-in flux is not required to be equal to the flow-out flux for each metabolite. In addition, we observed that the flux rates of biomass synthesis and the TCA cycle gradually increase as the iPSCs reach the stationary phase from the exponential phase. A similar observation is also reported by the literature study Templeton et al. (2013).

Table 1 lists the prediction of consumption and production rates for the critical extracellular metabolites. The experimentally determined 12-h to 36-h biomass-specific uptake and production rates based on the Extracellular Time-Course Analysis (ETA) software (Murphy and Young, 2013) are also provided for comparison. Notice ETA results are based on metabolic steady-state assumption, which explains the reason that most ETA prediction of metabolites at 12-h to 36-h is located between the predictions of metabolites at 24-h and 48-h obtained by using the developed metabolic kinetic model. Under limited substrate conditions, the consumption rate changes significantly, as seen with glucose on LGHL and LGHL, and pyruvate on all four conditions. In contrast to methodologies based on the metabolic steady-state assumption, the proposed metabolic kinetic model captures these critical dynamic behaviors, which can facilitate the development of bioprocess control.

Moreover, the results presented in Table 1 are consistent with the regulatory mechanisms outlined in Section 3.3. Specifically, the consumption rate of glucose increases with higher extracellular glucose concentration (e.g., HGHL vs.

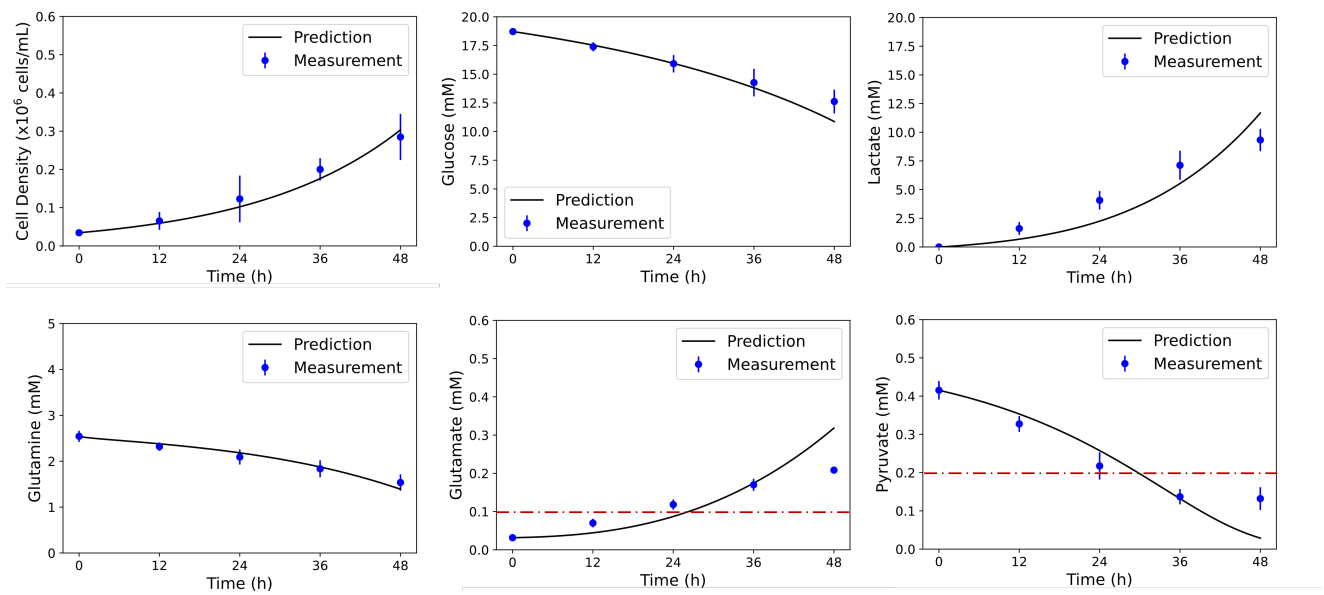


Figure 4: Cell characteristic predictions for the high glucose and low lactate cultures using the dynamic model trained on the other three case data sets. (A) Cell density, (B) Glucose, (C) Lactate, (D) Glutamine, (E) Glutamate, and (F) Pyruvate. The detection limit of the Cedex Bioanalyzer is shown as the red dash-dot line.

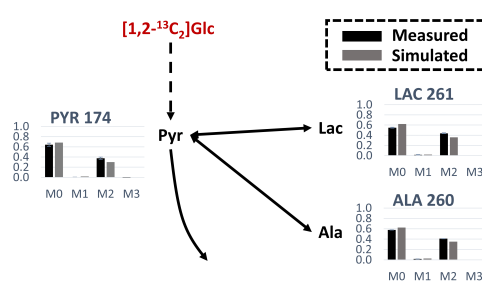


Figure 5: MID pattern predictions from the $[1,2-^{13}\text{C}_2]$ glucose tracer at 48-h for control (HGLL) cultures using the dynamic model trained on the other three data sets compared to literature measurements. MIDs shown have been corrected for natural abundance.

LGHL and HGHL vs. LGHL), while it decreases with higher extracellular lactate concentration (e.g., HGHL vs. HGHL and LGHL vs. LGHL), which is attributed to regulatory mechanism **R1** in eq (7). For lactate, the net production rate is lower when a certain amount of lactate exists in the cultural environment (see HGHL v.s. HGHL and LGHL v.s. LGHL). For pyruvate, in high lactate culture conditions, more favorable lactate transport kinetics of MCTs decreases pyruvate consumption (see HGHL v.s. HGHL and LGHL v.s. LGHL). This is associated with regulatory mechanism **R6** in eq (12). As the lactate dampens the conversion of glutamine to glutamate, under high lactate culture conditions, the consumption rate of glutamine and production rate of glutamate decrease (see HGHL v.s. HGHL and LGHL v.s.

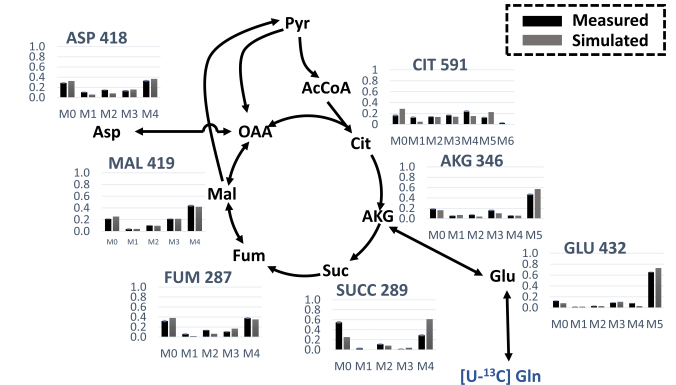


Figure 6: MID pattern predictions from the $[U-^{13}\text{C}_5]$ glutamine tracer at 48-h for control (HGLL) cultures using the dynamic model trained on the other three data sets compared to literature measurements. MIDs shown have been corrected for natural abundance.

LGHL). This is associated with regulatory mechanisms **R2** in eq (8) and **R7** in eq (13). The ability of the proposed model to accurately predict dynamic cell behavior under environmental perturbations further confirms its reliability.

5. Conclusions

In this paper, we create a metabolic kinetic model characterizing the time-variate dynamics and regulatory mechanisms of the iPSC culture process. This model mainly focuses on central carbon metabolism, including glycolysis, TCA cycle, PPP, anaplerosis, and key amino acid metabolism. The created iPSC metabolic regulatory network simulator is calibrated by using the experimental data on

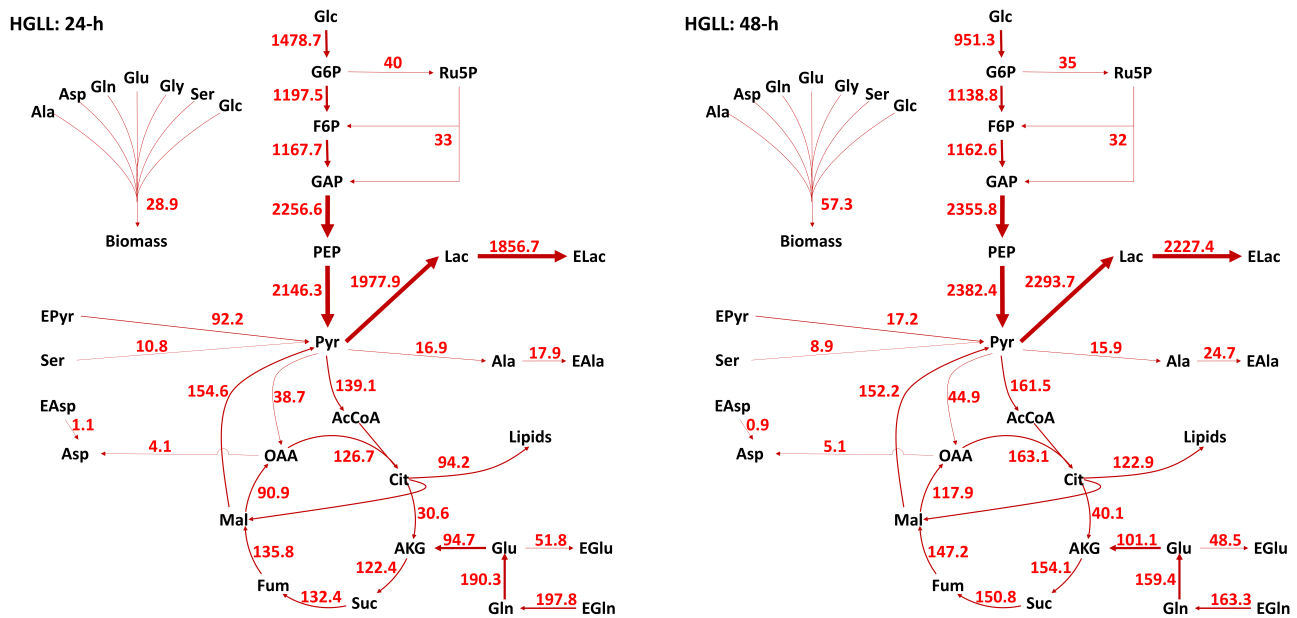


Figure 7: Metabolic flux maps for K3 iPSC for the high glucose and low lactate cultures at 24-h and 48-h. Predicted fluxes are given in nmol/10⁶ cells·h. The line thicknesses represent the relative fluxes.

Table 1

Dynamic model prediction for biomass-specific uptake and production rates for key extracellular metabolite (nmol/10⁶ cells·h). The fluxes obtained by Extracellular Time-Course Analysis (ETA) for 12-h to 36-h are calculated averages from measurements (Odenwelder et al., 2021), while the 24-h and 36-h fluxes predicted by the developed metabolic kinetic model are calculated for that specific time point. Negative values represent consumption rates and positive values represent production rates.

Metabolite	HGLL (nmol/10 ⁶ cells·h)			LGHL (nmol/10 ⁶ cells·h)		
	24-h	48-h	12-h to 36-h (ETA)	24-h	48-h	12-h to 36-h (ETA)
Glucose	-1,478.7	-951.3	-1,051	-1,247.9	-255.3	-994
Lactate	1,856.7	2,227.4	2,108	1,830.3	1,701.3	2,000
Pyruvate	-92.1	-17.2	-67.7	-93.8	-18.5	-75.2
Glutamate	50.1	48.5	36.2	51.3	52.8	32.4
Glutamine	-197.8	-163.3	-132	-197.3	-160.4	-147
HGHL (nmol/10 ⁶ cells·h)						
Metabolite	24-h	48-h	12-h to 36-h (ETA)	24-h	48-h	12-h to 36-h (ETA)
Glucose	-828.9	-703.1	-874	-710.3	-493.6	-860
Lactate	1,522	1,459.9	1,694	1,420	1,119.7	1,651
Pyruvate	-65.2	-32.3	-39	-65.9	-33.9	-36.5
Glutamate	45.8	44.1	28.3	46.4	48.1	29.4
Glutamine	-175.2	-148.1	-107	-175.4	-148.1	-120

extracellular metabolite concentrations and intracellular isotopic measurements from multiple tracers (i.e., [1,2-¹³C₂] glucose, [U-¹³C₅] glutamine and [U-¹³C₃] sodium L-lactate tracers). These time-course measurements are collected heterogeneously at multiple time points along the cell culture process under different conditions (i.e., different levels of extracellular glucose and lactate concentrations). Both the capacities of iPSC culture process trajectory prediction under the same experimental initial condition and extrapolation across different initial conditions are assessed by using experimental measures. The developed metabolic kinetic model shows promising results and it provides a reliable

prediction of stem cellular metabolic response to extracellular glucose and lactate concentration's perturbation. It can advance the understanding of the iPSC culture intracellular regulatory mechanisms, improve the capability for real-time cell culture process monitoring, and support optimal control for integrated iPSC culture processes.

References

- Ahn, W.S., Antoniewicz, M.R., 2011. Metabolic flux analysis of CHO cells at growth and non-growth phases using isotopic tracers and mass spectrometry. *Metabolic engineering* 13, 598–609.
- Ahn, W.S., Antoniewicz, M.R., 2013. Parallel labeling experiments with [1, 2-¹³C] glucose and [¹³C] glutamine provide new insights into CHO cell metabolism. *Metabolic engineering* 15, 34–47.
- Antoniewicz, M.R., 2015. Methods and advances in metabolic flux analysis: a mini-review. *Journal of Industrial Microbiology and Biotechnology* 42, 317–325.
- Antoniewicz, M.R., 2018. A guide to ¹³C metabolic flux analysis for the cancer biologist. *Experimental & molecular medicine* 50, 1–13.
- Antoniewicz, M.R., 2021. A guide to metabolic flux analysis in metabolic engineering: Methods, tools and applications. *Metabolic engineering* 63, 2–12.
- Antoniewicz, M.R., Kelleher, J.K., Stephanopoulos, G., 2007. Elementary metabolite units (EMU): a novel framework for modeling isotopic distributions. *Metabolic engineering* 9, 68–86.
- Chang, A., Jeske, L., Ulbrich, S., Hofmann, J., Koblitz, J., Schomburg, I., Neumann-Schaal, M., Jahn, D., Schomburg, D., 2021. BRENDA, the ELIXIR core data resource in 2021: new developments and updates. *Nucleic acids research* 49, D498–D508.
- Costa Leite, T., Da Silva, D., Guimarães Coelho, R., Zancan, P., Sola-Penna, M., 2007. Lactate favours the dissociation of skeletal muscle 6-phosphofructo-1-kinase tetramers down-regulating the enzyme and muscle glycolysis. *Biochemical Journal* 408, 123–130.
- Draoui, N., Feron, O., 2011. Lactate shuttles at a glance: from physiological paradigms to anti-cancer treatments. *Disease models & mechanisms* 4, 727–732.
- Dressel, R., 2011. Effects of histocompatibility and host immune responses on the tumorigenicity of pluripotent stem cells, in: *Seminars in immunopathology*, Springer. p. 573.
- Fiorenza, S., Ritchie, D.S., Ramsey, S.D., Turtle, C.J., Roth, J.A., 2020. Value and affordability of CAR T-cell therapy in the United States. *Bone marrow transplantation* 55, 1706–1715.
- Ghorbaniaghdam, A., Chen, J., Henry, O., Jolicoeur, M., 2014a. Analyzing clonal variation of monoclonal antibody-producing CHO cell lines using an *in silico* metabolomic platform. *PloS one* 9, e90832.
- Ghorbaniaghdam, A., Henry, O., Jolicoeur, M., 2013. A kinetic-metabolic model based on cell energetic state: study of CHO cell behavior under Na-butyrate stimulation. *Bioprocess and biosystems engineering* 36, 469–487.
- Ghorbaniaghdam, A., Henry, O., Jolicoeur, M., 2014b. An *in-silico* study of the regulation of CHO cells glycolysis. *Journal of theoretical biology* 357, 112–122.
- Glacken, M., Adema, E., Sinskey, A., 1988. Mathematical descriptions of hybridoma culture kinetics: I. Initial metabolic rates. *Biotechnology and bioengineering* 32, 491–506.
- Halestrap, A.P., 2012. The monocarboxylate transporter family-structure and functional characterization. *IUBMB life* 64, 1–9.
- Hanna, E., Rémuazat, C., Auquier, P., Toumi, M., 2016. Advanced therapy medicinal products: current and future perspectives. *Journal of market access & health policy* 4, 31036.
- Hassell, T., Gleave, S., Butler, M., 1991. Growth inhibition in animal cell culture: The effect of lactate and ammonia. *Applied biochemistry and biotechnology* 30, 29–41.
- Huckabee, W.E., 1956. Control of concentration gradients of pyruvate and lactate across cell membranes in blood. *Journal of Applied Physiology* 9, 163–170.
- Ivarsson, M., Noh, H., Morbidelli, M., Soos, M., 2015. Insights into pH-induced metabolic switch by flux balance analysis. *Biotechnology Progress* 31, 347–357.
- Jazmin, L.J., Young, J.D., 2013. Isotopically nonstationary ¹³C metabolic flux analysis. *Systems Metabolic Engineering: Methods and Protocols*, 367–390.
- Kinney, M.A., Sargent, C.Y., McDevitt, T.C., 2011. The multiparametric effects of hydrodynamic environments on stem cell culture. *Tissue Engineering Part B: Reviews* 17.
- Kyriakopoulos, S., Ang, K.S., Lakshmanan, M., Huang, Z., Yoon, S., Guanwan, R., Lee, D.Y., 2018. Kinetic modeling of mammalian cell culture bioprocessing: the quest to advance biomanufacturing. *Biotechnology Journal* 13, 1700229.
- Leighty, R.W., Antoniewicz, M.R., 2011. Dynamic metabolic flux analysis (DMFA): a framework for determining fluxes at metabolic non-steady state. *Metabolic engineering* 13, 745–755.
- Mulukutla, B.C., Gramer, M., Hu, W.S., 2012. On metabolic shift to lactate consumption in fed-batch culture of mammalian cells. *Metabolic engineering* 14, 138–149.
- Murphy, T.A., Young, J.D., 2013. ETA: robust software for determination of cell specific rates from extracellular time courses. *Biotechnology and bioengineering* 110, 1748–1758.
- Nelson, D.L., Lehninger, A.L., Cox, M.M., 2008. *Lehninger principles of biochemistry*. Macmillan.
- Niklas, J., Heinzle, E., 2012. Metabolic flux analysis in systems biology of mammalian cells. *Genomics and Systems Biology of Mammalian Cell Culture*, 109–132.
- Nolan, R.P., Lee, K., 2011. Dynamic model of CHO cell metabolism. *Metabolic engineering* 13, 108–124.
- Odenwelder, D.C., Lu, X., Harcum, S.W., 2021. Induced pluripotent stem cells can utilize lactate as a metabolic substrate to support proliferation. *Biotechnology Progress* 37, e3090.
- Rivera-Ordaz, A., Peli, V., Manzini, P., Barilani, M., Lazzari, L., 2021. Critical Analysis of cGMP Large-Scale Expansion Process in Bioreactors of Human Induced Pluripotent Stem Cells in the Framework of Quality by Design. *BioDrugs* 35, 693–714.
- Sengupta, N., Rose, S.T., Morgan, J.A., 2011. Metabolic flux analysis of CHO cell metabolism in the late non-growth phase. *Biotechnology and bioengineering* 108, 82–92.
- Stephanopoulos, G., Aristidou, A.A., Nielsen, J., 1998. Metabolic engineering: principles and methodologies .
- Templeton, N., Dean, J., Reddy, P., Young, J.D., 2013. Peak antibody production is associated with increased oxidative metabolism in an industrially relevant fed-batch CHO cell culture. *Biotechnology and bioengineering* 110, 2013–2024.
- Wang, L.L.W., Janes, M.E., Kumbhojkar, N., Kapate, N., Clegg, J.R., Prakash, S., Heavey, M.K., Zhao, Z., Anselmo, A.C., Mitragotri, S., 2021. Cell therapies in the clinic. *Bioengineering & translational medicine* 6, e10214.
- Young, J.D., Walther, J.L., Antoniewicz, M.R., Yoo, H., Stephanopoulos, G., 2008. An elementary metabolite unit (emu) based method of isotopically nonstationary flux analysis. *Biotechnology and bioengineering* 99, 686–699.

A. Appendix: Table

The following tables summarize detailed information about the constructed iPSC metabolic network and developed kinetic model.

- The iPSC metabolic network contains the major reactions for glycolysis, the TCA cycle, anaplerosis, PPP, and amino acid metabolism; see the specific reactions in Table 2. The reactions of PPP are collapsed into two: Oxidative phase/branch and Non-oxidative phase/branch (i.e., No. 9 & 10 reactions).
- The iPSC metabolic flux rate regulation biokinetic model is summarized in Table 3. Key activators and inhibitors are considered for each reaction, and their impact on the regulatory mechanisms is characterized through Michaelis–Menten model.
- The descriptions of the metabolites, considered in the developed metabolic kinetic model, are listed in Table 4.
- For the developed metabolic kinetic model, the descriptions of the enzymes with Enzyme Commission Number (EC-No.) are provided in Table 5. They are associated with metabolic flux reaction rates.

Table 2

Reactions of the metabolic network

No.	Pathway
Glycolysis	
1	Glc(abcdef) → G6P(abcdef)
2	G6P(abcdef) → F6P(abcdef)
3	F6P(abcdef) → GAP(cba) + GAP (def)
4	GAP(abc) → PEP(abc)
5	PEP(abc) → Pyr(abc)
6	Pyr(abc) ↔ Lac(abc)
7	EPyr(abc) → Pyr(abc)
8	Lac(abc) ↔ ELac(abc)
PPP	
9	G6P(abcdef) → Ru5P(bcdef)+CO ₂ (a)
10	Ru5P(abcd) + Ru5P(fghij) + Ru5P(klmno) → F6P(fgahij) + F6P(klbcde) + GAP(mno)
TCA	
11	Pyr(abc) → AcCoA(bc)+CO ₂ (a)
12	AcCoA(ab)+OAA(cdef) → Cit(fedbac)
13	Cit(abcdef) ↔ AKG(abcde) + CO ₂ (f)
14	AKG(abcde) → Suc(bcde) + CO ₂ (a)
15	Suc(abcd) → Fum(abcd)
16	Fum(abcd) ↔ Mal(abcd)
17	Mal(abcd) ↔ OAA(abcd)
Anaplerosis and Amino Acid	
18	Mal(abcd) → Pyr(abc)+CO ₂ (d)
19	Pyr(abc) +CO ₂ (d) → OAA(abcd)
20	Gln(abcde) ↔ Glu(abcde)+NH ₄
21	Glu(abcde)↔ AKG(abcde)+NH ₄
22	Glu(abcde)+Pyr(fgh)↔ AKG(abcde)+Ala(fgh)
23	Ala(abc) → EAla(abc)
24	Glu(abcde) → EGlu(abcde)
25	EGln(abcde) → Gln(abcde)
26	Ser(abc) → Pyr(abc)+ NH ₄
27	Asp(fghi)+AKG(abcde) ↔ Glu(abcde)+OAA(fghi)+NH ₄
28	EAsp(abcd) → Asp(abcd)
29	Cit(abcdef) → Mal(fcba) + Lipids
Biomass	
30	0.19 Ala + 0.11 Asp + 0.1 Gln + 0.12 Glu + 0.17 Gly + 0.14 Ser + 0.16 Glc → Biomass

Table 3

Biokinetic equations of the metabolites fluxes (1-30) of the model

No.	Pathway
Glycolysis	
1	$v(HK) = v_{max,HK} \times \frac{Glc}{K_{m,Glc}+Glc} \times \frac{K_{i,G6P}}{K_{i,G6P}+G6P} \times \frac{K_{i,LactoHK}}{K_{i,LactoHK}+Lac}$
2	$v(PGI) = v_{max,PGI} \times \frac{G6P}{K_{m,G6P}+G6P}$
3	$v(PFK/ALD) = v_{max,PFK/ALD} \times \frac{F6P}{K_{m,F6P}+F6P}$
4	$v(PGK) = v_{max,PGK} \times \frac{GAP}{K_{m,GAP}+GAP}$
5	$v(PK) = v_{max,PK} \times \frac{PEP}{K_{m,PEP} \times (1 + \frac{K_{a,F6P}}{F6P}) + PEP}$
6f	$vLDHf = v_{max,fLDH} \times \frac{Pyr}{K_{m,Pyr}+Pyr}$
6r	$v(LDHR) = v_{max,rLDH} \times \frac{Lac}{K_{m,Lac}+Lac} \times \frac{K_{i,Pyr}}{K_{i,Pyr}+Pyr}$
7	$v(PyrT) = v_{max,PyrT} \times \frac{E Pyr}{K_{m,E Pyr}+E Pyr} \times \frac{K_{i,LactoPyr}}{K_{i,LactoPyr}+Lac}$
8f	$v(LacTf) = v_{max,fLacT} \times \frac{Lac}{K_{m,Lac}+Lac}$
8r	$v(LacTr) = v_{max,rLacT} \times \frac{ELac}{K_{m,ELac}+ELac}$
PPP	
9	$v(OP) = v_{max,OP} \times \frac{G6P}{K_{m,G6P}+G6P}$
10	$v(NOP) = v_{max,NOP} \times \frac{Ru5P}{K_{m,Ru5P}+Ru5P}$
TCA	
11	$v(PDH) = v_{max,PDH} \times \frac{Pyr}{K_{m,Pyr}+Pyr}$
12	$v(CS) = v_{max,CS} \times \frac{AcCoA}{K_{m,AcCoA}+AcCoA} \times \frac{OAA}{K_{m,OAA}+OAA}$
13f	$v(CITS/ISODf) = v_{max,fCITS/ISOD} \times \frac{Cit}{K_{m,Cit}+Cit}$
13r	$v(CITS/ISODr) = v_{max,rCITS/ISOD} \times \frac{AKG}{K_{m,AKG}+AKG}$
14	$v(AKGDH) = v_{max,AKGDH} \times \frac{AKG}{K_{m,AKG}+AKG}$
15	$v(SDH) = v_{max,SDH} \times \frac{Suc}{K_{m,Suc}+Suc}$
16f	$v(FUMf) = v_{max,fFUM} \times \frac{Fum}{K_{m,Fum}+Fum}$
16r	$v(FUMr) = v_{max,rFUM} \times \frac{Mal}{K_{m,Mal}+Mal}$
17f	$v(MDHf) = v_{max,fMDH} \times \frac{Mal}{K_{m,Mal}+Mal}$
17r	$v(MDHr) = v_{max,rMDH} \times \frac{OAA}{K_{m,OAA}+OAA}$

Anaplerosis and Amino Acid	
18	$v(ME) = v_{max,ME} \times \frac{Mal}{K_m, Mal + Mal}$
19	$v(PC) = v_{max,PC} \times \frac{Pyr}{K_m, Pyr + Pyr}$
20f	$v(GLNSf) = v_{max,fGLNS} \times \frac{Gln}{K_m, Gln + Gln} \times \frac{K_i, LactoGLNS}{K_i, LactoGLNS + Lac}$
20r	$v(GLNSr) = v_{max,rGLNS} \times \frac{Glu}{K_m, Glu + Glu} \times \frac{NH_4}{K_m, NH_4 + NH_4}$
21f	$v(GLDHf) = v_{max,fGLDH} \times \frac{Glu}{K_m, Glu + Glu}$
21r	$v(GLDHR) = v_{max,rGLDH} \times \frac{AKG}{K_m, AKG + AKG} \times \frac{NH_4}{K_m, NH_4 + NH_4}$
22f	$v(AlaTAf) = v_{max,fAlaTA} \times \frac{Glu}{K_m, Glu + Glu} \times \frac{Pyr}{K_m, Pyr + Pyr}$
22r	$v(AlaTAr) = v_{max,rAlaTA} \times \frac{Ala}{K_m, Ala + Ala} \times \frac{AKG}{K_m, AKG + AKG} \times (1 + \frac{K_a, Gln}{Gln})$
23	$v(AlaT) = v_{max,AlaT} \times \frac{Ala}{K_m, Ala + Ala}$
24	$v(GluT) = v_{max,GluT} \times \frac{Glu}{K_m, Glu + Glu}$
25	$v(GlnT) = v_{max,GlnT} \times \frac{EGln}{K_m, EGln + EGln} \times \frac{K_i, GLN}{K_i, GLN + GLN}$
26	$v(SAL) = v_{max,SAL} \times \frac{Ser}{K_m, Ser + Ser}$
27f	$v(ASTAf) = v_{max,fASTA} \times \frac{Asp}{K_m, ASP + Asp} \times \frac{AKG}{K_m, AKG + AKG}$
27r	$v(ASTAr) = v_{max,rASTA} \times \frac{Glu}{K_m, Glu + Glu} \times \frac{OAA}{K_m, OAA + OAA} \times \frac{NH_4}{K_m, NH_4 + NH_4}$
28	$v(AspT) = v_{max,AspT} \times \frac{EAsp}{K_m, EAsp + EAsp}$
29	$v(ACL) = v_{max,ACL} \times \frac{Cit}{K_m, Cit + Cit}$
Biomass	
30	$v(growth) = v_{max,growth} \times \frac{Gln}{K_m, Gln + Gln} \times \frac{Glc}{K_m, Glc + Glc} \times \frac{Glu}{K_m, Glu + Glu} \times \frac{Ala}{K_m, Ala + Ala} \times \frac{Asp}{K_m, Asp + Asp} \times \frac{Ser}{K_m, Ser + Ser} \times \frac{Gly}{K_m, Gly + Gly}$

Table 4
Description of the Metabolite

Component	Description	Component	Description
ACCoA	Acetyl-CoenzymeA	ALA	Alanine
AKG	α -Ketoglutarate	ASP	Aspartate
CIT	Citrate	LAC	Lactate
CO2	Intracellular Carbonoxygen	GLN	Glutamine
F6P	Fructose 6-Phosphate	EGLY	Extracellular Glycine
G6P	Glucose 6-Phosphate	SER	Extracellular Serine
GAP	Glyceraldehyde 3-Phosphate	GLC	Extracellular Glucose
GLU	Glutamate	EGLN	Extracellular Glutamine
GLY	Glycine	EGLU	Extracellular Glutamate
MAL	Malate	EPYR	Extracellular Pyruvate
OAA	Oxaloacetate	EASP	Extracellular Aspartate
PEP	Phosphoenolpyruvate	EALA	Extracellular Alanine
FUM	Fumarate	ELAC	Extracellular Lactate
Ru5P	Ribulose 5-Phosphate	NH4	Extracellular Ammonia
SUC	Succinate	LIPID	Lipid
PYR	Pyruvate	Bio	Biomass

Table 5
Description of the Enzyme

Abbreviation	Description	EC-No.
HK	Hexokinase	2.7.1.1
PGI	Phosphoglucose Isomerase	5.3.1.9
PFK/ALD	Phosphofructokinase/Aldolase	2.7.1.11/4.1.2.13
PGK	Phosphoglycerate Kinase	2.7.2.3
PK	Pyruvate Kinase	2.7.1.40
OP	Oxidative Phase of PPP	
NOP	Non-oxidative Phase of PPP	
PyrT	Membrane Transport of Pyruvate	
SAL	Membrane Transport of Serine	
LDH	Lactate Dehydrogenase	1.1.1.27
AlaTA	Alanine Transaminase	2.6.1.2
PC	Pyruvate Carboxylase	6.4.1.1
PDH	Pyruvate Dehydrogenase	1.2.4.1
CS	Citrate (Si)-Synthase	2.3.3.1
CITS/ISOD	Aconitase/Isocitrate Dehydrogenase	4.2.1.3/1.1.1.41
GLDH	Glutamate Dehydrogenase	1.4.1.2
GluT	Membrane Transport of Glutamate	
GLNS	Glutamine Synthetase	6.3.1.2
AKGDH	α -ketoglutarate Dehydrogenase	1.2.1.105
SDH	Succinate Dehydrogenase	1.3.5.1
MDH	Malate Dehydrogenase	1.1.1.37
ME	Malic Enzyme	1.1.1.40
ASTA	Aspartate Aminotransferase	2.6.1.1
ACL	ATP citrate synthase	2.3.3.8
FUM	Fumarase	4.2.1.2

B. Appendix: Cell Characteristic Predictions

Fig. 8 to 10 depict the model prediction results of the iPSC culture process for three cases with different initial conditions, including high glucose and high lactate (HGHL), low glucose and low lactate (LGLL), and low glucose and high lactate cultures (LGHL) respectively.

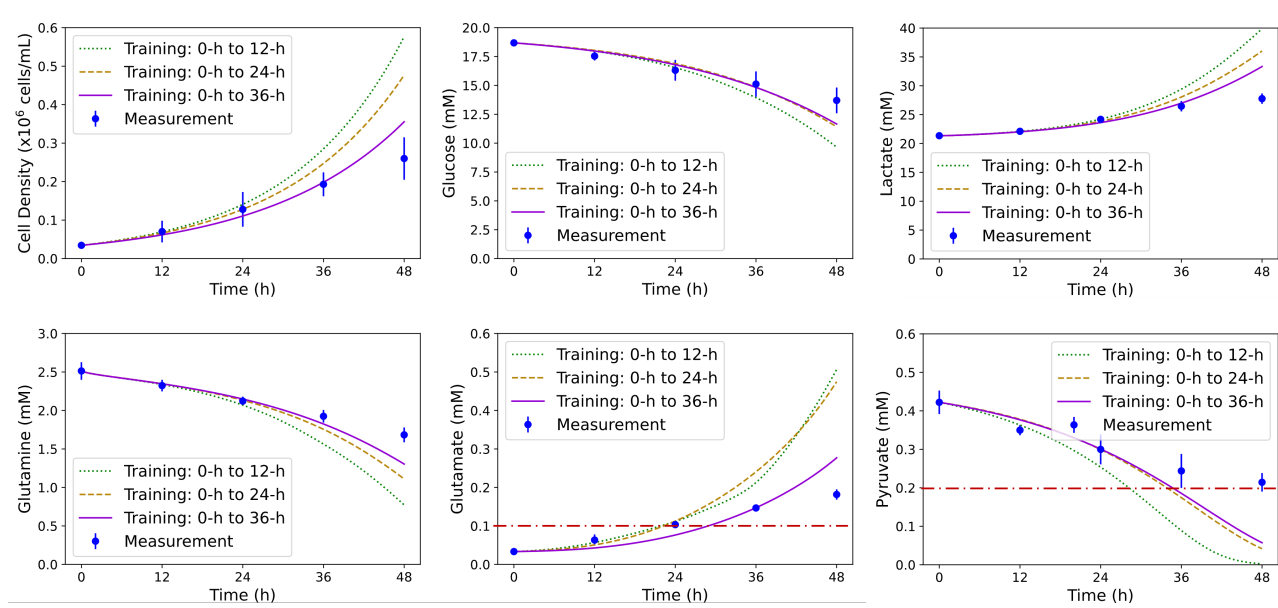


Figure 8: Cell characteristic predictions for the high glucose and high lactate cultures using the dynamic model trained on different time intervals. (A) Cell density, (B) Glucose, (C) Lactate, (D) Glutamine, (E) Glutamate, and (F) Pyruvate. Times 0-h to 12-h (green dotted line); Times 0-h to 24-h (brown dashed line); and Times 0-h to 36-h (purple solid line). The detection limit of the Cedex Bioanalyzer is shown as the red dash-dot line.

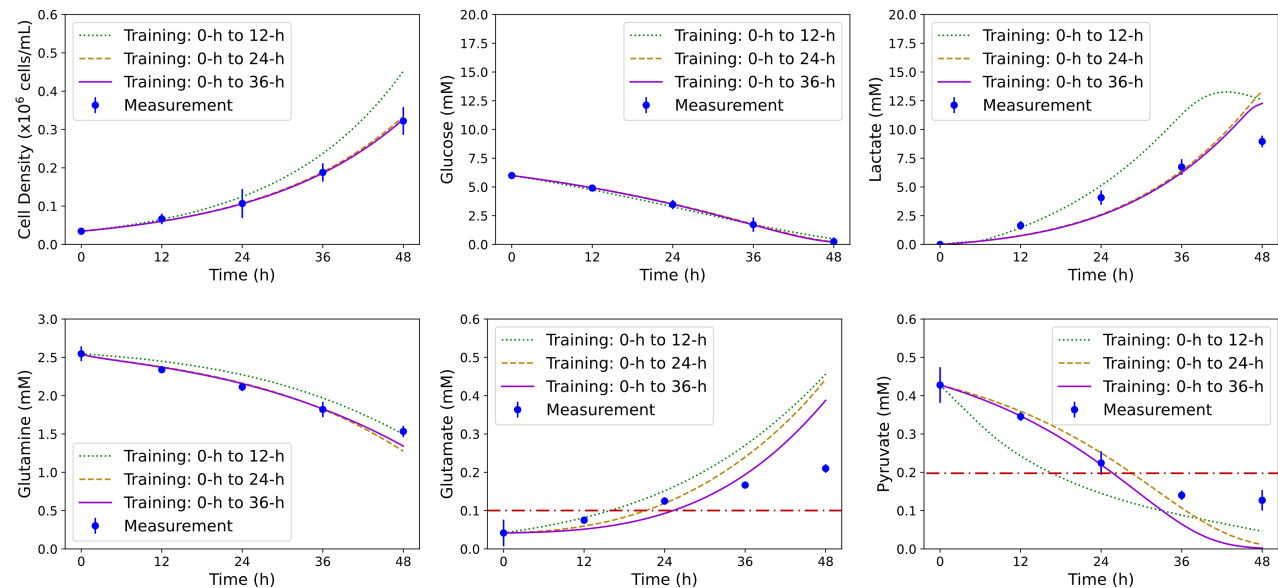


Figure 9: Cell characteristic predictions for the low glucose and low lactate cultures using the dynamic model trained on different time intervals. (A) Cell density, (B) Glucose, (C) Lactate, (D) Glutamine, (E) Glutamate, and (F) Pyruvate. Times 0-h to 12-h (green dotted line); Times 0-h to 24-h (brown dashed line); and Times 0-h to 36-h (purple solid line). The detection limit of the Cedex Bioanalyzer is shown as the red dash-dot line.

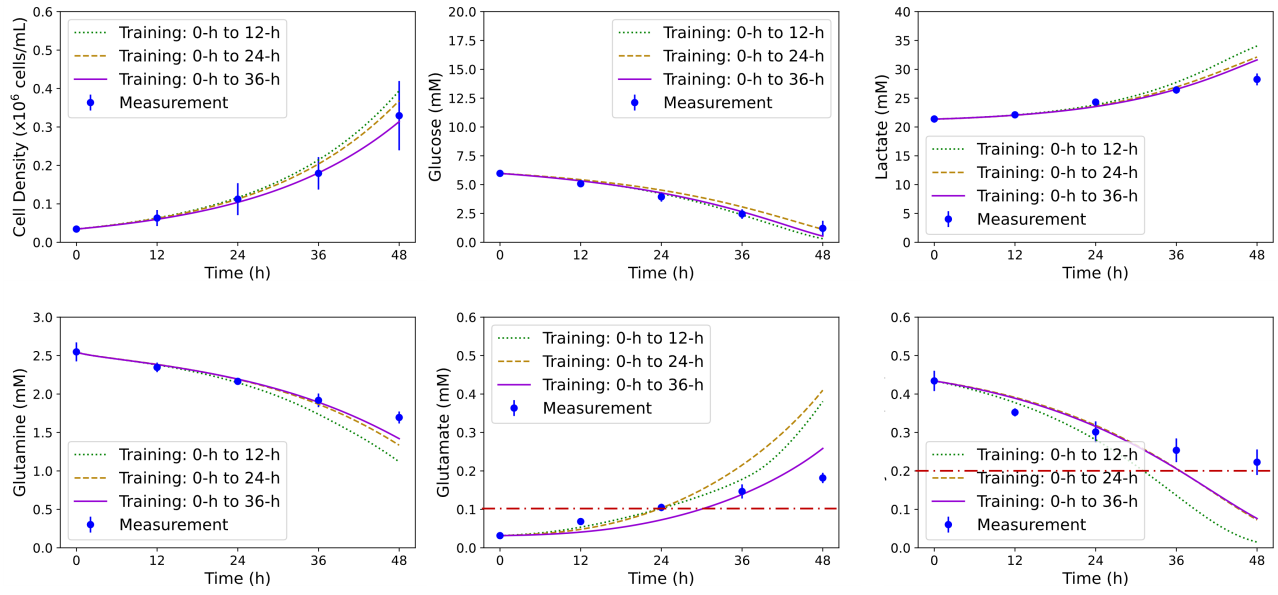


Figure 10: Cell characteristic predictions for the low glucose and high lactate cultures using the dynamic model trained on different time intervals. (A) Cell density, (B) Glucose, (C) Lactate, (D) Glutamine, (E) Glutamate, and (F) Pyruvate. Times 0-h to 12-h (green dotted line); Times 0-h to 24-h (brown dashed line); and Times 0-h to 36-h (purple solid line). The detection limit of the Cedex Bioanalyzer is shown as the red dash-dot line.

C. Appendix: Cell Characteristic Across Culture Condition Predictions

Fig. 11 to 13 depict the prediction results across different initial conditions for cases, including high glucose and high lactate (HGHL), low glucose and low lactate (LGLL), and low glucose and high lactate (LGHL) respectively. Basically, the model is fitted by using the data from the remaining three cases.

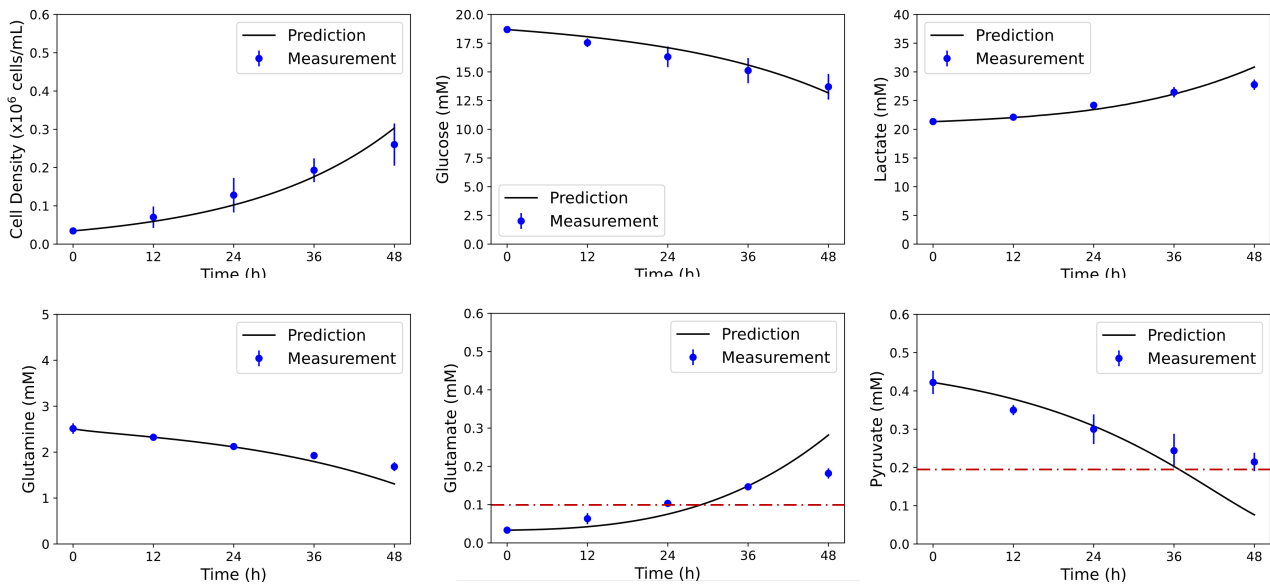


Figure 11: Cell characteristic predictions for the high glucose and high lactate cultures using the dynamic model trained on the other three case data sets. (A) Cell density, (B) Glucose, (C) Lactate, (D) Glutamine, (E) Glutamate, and (F) Pyruvate. The detection limit of the Cedex Bioanalyzer is shown as the red dash-dot line.

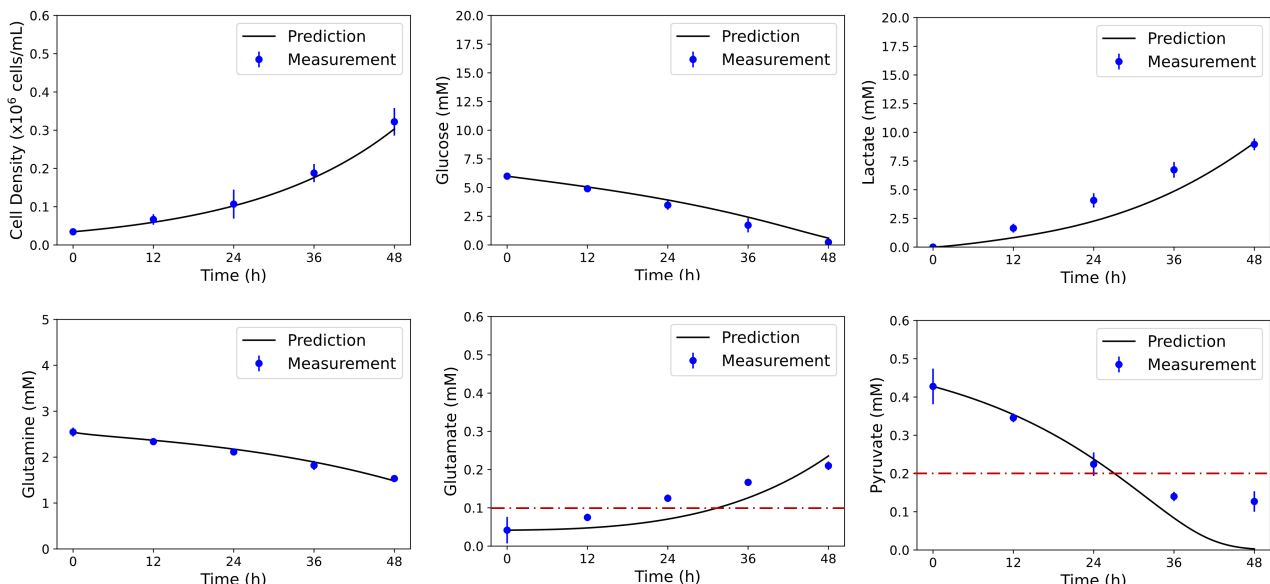


Figure 12: Cell characteristic predictions for the low glucose and low lactate cultures using the dynamic model trained on the other three case data sets. (A) Cell density, (B) Glucose, (C) Lactate, (D) Glutamine, (E) Glutamate, and (F) Pyruvate. The detection limit of the Cedex Bioanalyzer is shown as the red dash-dot line.

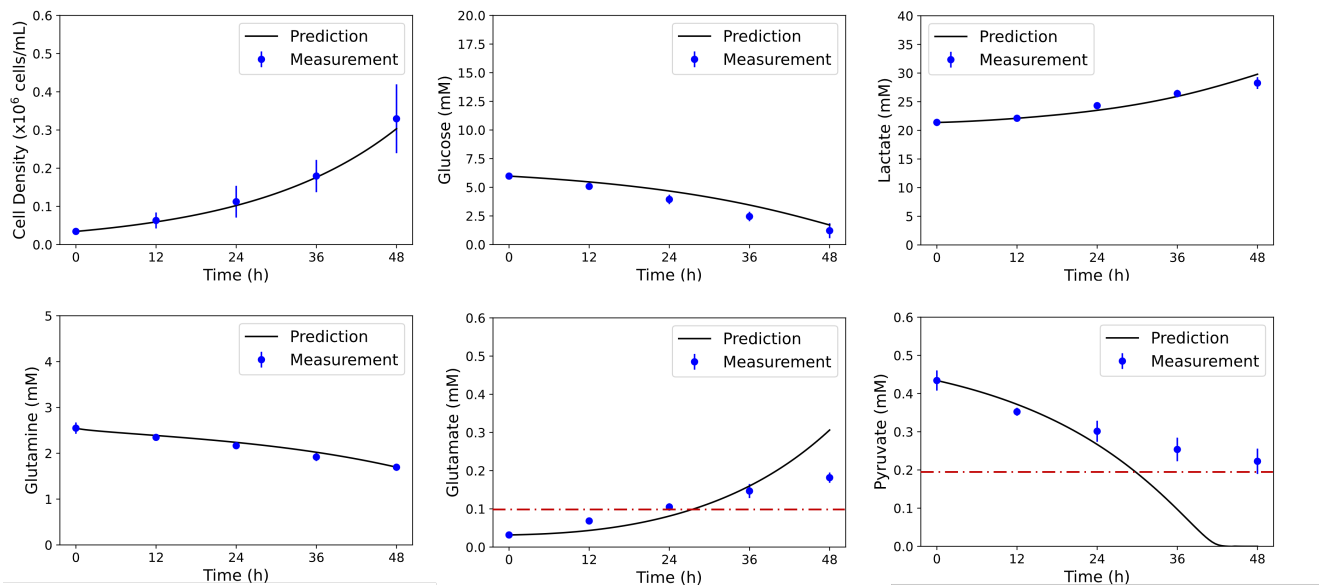


Figure 13: Cell characteristic predictions for the low glucose and high lactate cultures using the dynamic model trained on the other three case data sets. (A) Cell density, (B) Glucose, (C) Lactate, (D) Glutamine, (E) Glutamate, and (F) Pyruvate. The detection limit of the Cedex Bioanalyzer is shown as the red dash-dot line.

D. Appendix: Metabolic flux maps

Fig 14 to 16 depict the metabolic flux maps for iPSC culture at 24-h and 48-h respectively under the initial conditions, including high glucose and high lactate (HGHL), low glucose and low lactate (LGLL), and low glucose and high lactate (LGHL).

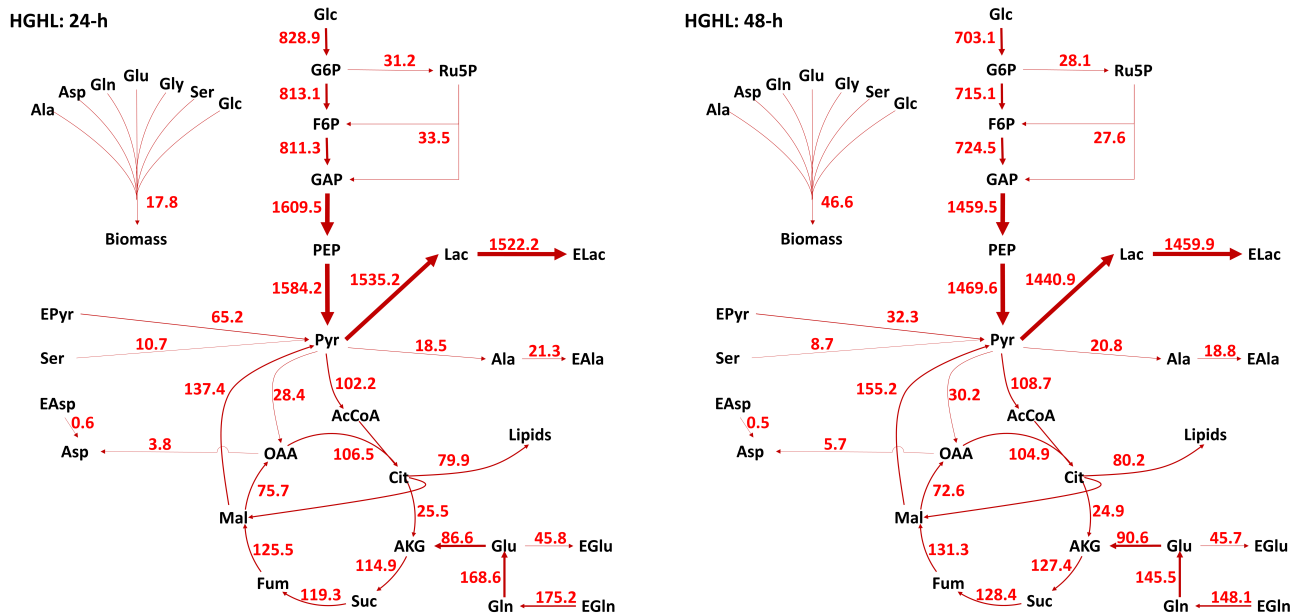


Figure 14: Metabolic flux maps for K3 iPSC for the high glucose and high lactate cultures at 24-h and 48-h. Predicted fluxes are given in nmol/10⁶ cells·h. The line thicknesses represent the relative fluxes.

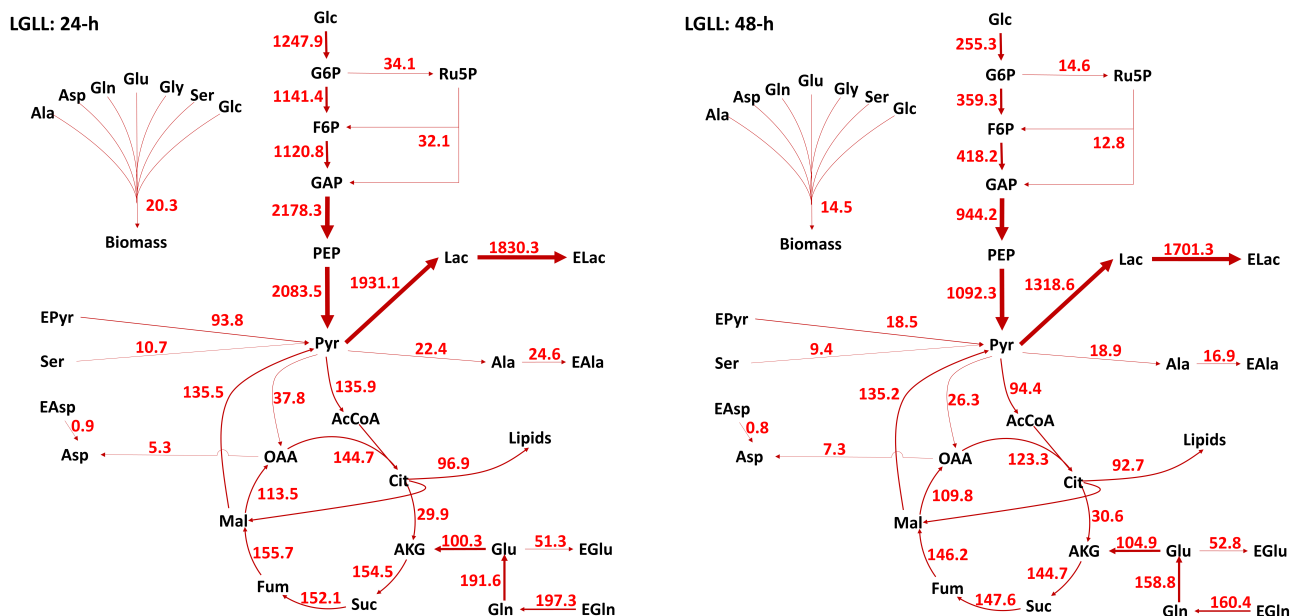


Figure 15: Metabolic flux maps for K3 iPSC for the low glucose and low lactate cultures at 24-h and 48-h. Predicted fluxes are given in nmol/10⁶ cells·h. The line thicknesses represent the relative fluxes.

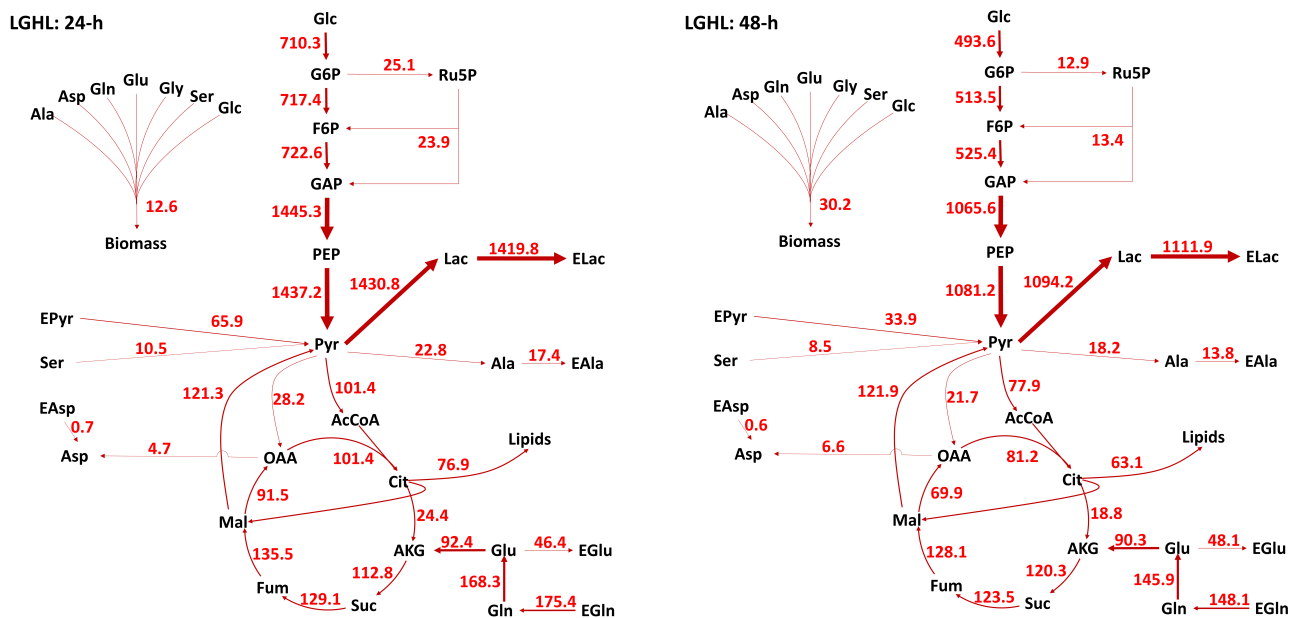


Figure 16: Metabolic flux maps for K3 iPSC for the low glucose and high lactate cultures at 24-h and 48-h. Predicted fluxes are given in nmol/10⁶ cells·h. The line thicknesses represent the relative fluxes.